

## Electronic Supplementary Information

### **Angle-dependent strength of a single chemical bond by stereographic force spectroscopy**

Wanhao Cai, Jakob T. Bullerjahn, Max Lallemand, Klaus Kroy,

Bizan N. Balzer,<sup>\*</sup> and Thorsten Hugel<sup>\*</sup>

#### **Contents**

<b>Reconstruction of curves along the pulling direction .....</b>	<b>2</b>
<b>Analysis of various effects in stereographic pulling.....</b>	<b>3</b>
<b>Single-chain elasticity model.....</b>	<b>8</b>
<b>Normalization of the polymer extension .....</b>	<b>10</b>
<b>Rupture force data analysis .....</b>	<b>14</b>
<b>References.....</b>	<b>21</b>

## Reconstruction of curves along the pulling direction

For the angle-dependent results, the force-extension curve of polyethylene glycol (PEG) along the pulling direction is reconstructed from the vertical component by  $F_p = F_z / \cos(\theta)$ ,  $R_p = R_z / \cos(\theta)$ . The latter is similar to  $R_p = \sqrt{R_z^2 + R_x^2}$  when the exerted forces and the stiffness of the cantilevers lead to a small amount of cantilever deflection compared to the  $z$ - and  $x$ -distances driven by the piezo system (see the *Analysis of various effects in stereographic pulling* on pages S3-S4). Then the curves are normalized using the two-state quantum mechanical freely rotating chain (TSQM-FRC) model curve (Eq. S5, black dotted line).

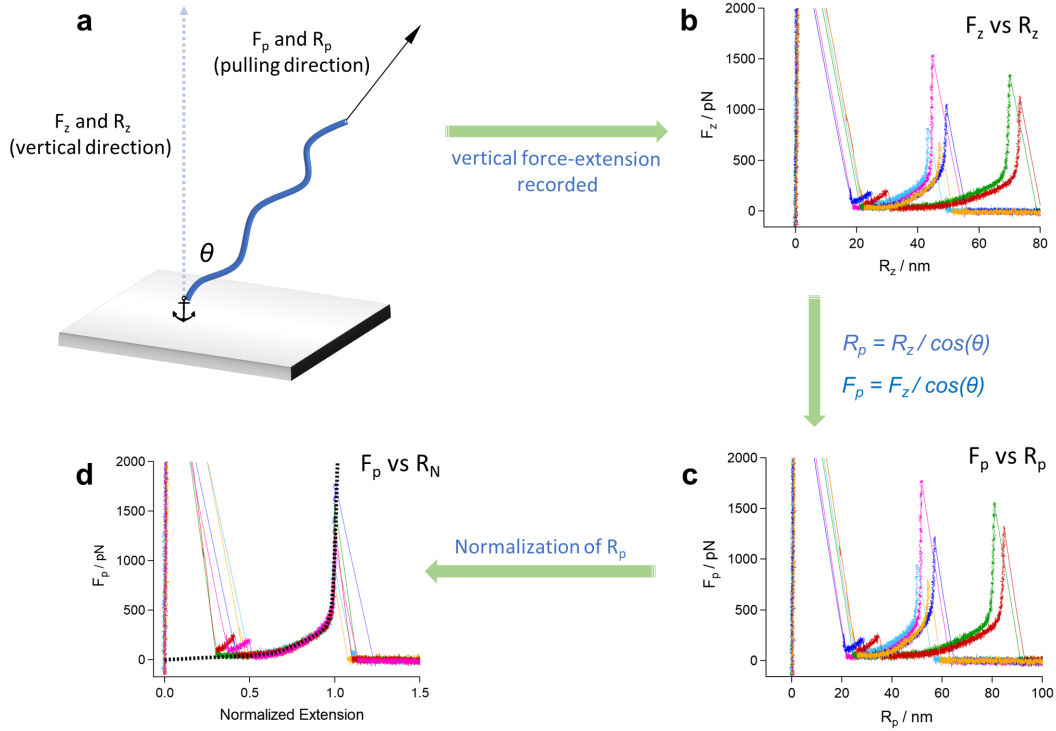


**Fig. S1 Reconstruction of force-extension curves to the pulling direction for stereographic pulling.** (a) Scheme of the experimental scenario. (b) Vertical force-extension curves ( $F_z$  vs  $R_z$ ) recorded by AFM. (c) Reconstructed force-extension curves ( $F_p$  vs  $R_p$ ) along the pulling direction. (d) Then, the extensions  $R_p$  are normalized using the TSQM-FRC model curve obtained from Eq. S5 ( $F_p$  vs normalized extension  $R_N$ , black dotted line). The exemplary curves shown are for  $\theta = 30^\circ$  at 100 nm/s in biotin-glass experiments.

## Analysis of various effects in stereographic pulling

Different types of effects could play a role in the stereographic pulling, which can lead to errors in the force measurements. These effects are analyzed as follows:

**Lateral deflection and torsion of the cantilever.** Here the surface is moved laterally (in its plane, but perpendicular to the cantilever axis) to avoid any torsion of the cantilever along the cantilever axis, in accordance with Kühner et al.<sup>1</sup> Furthermore, we find no significant lateral deflection or torsion perpendicular to the cantilever axis for the presented single molecule experiments due to a two or three orders of magnitude higher lateral force constant (Fig. S2), meaning that the lateral deflection and torsion perpendicular to the cantilever axis can also be ignored.<sup>2</sup>

**Vertical deflection of the cantilever.** The vertical deflection of a cantilever will cause a shorter  $z$ -extension of the polymer compared to the  $z$ -distance driven by the piezo system, especially for high forces this leads to a bias of the real pulling angle at the position of rupture compared to the intended pulling angle defined by the piezo driven  $z$ - and  $x$ -distances (Fig. S3a). This effect becomes stronger for steeper angles since the  $z$ -extension at the rupture force becomes shorter. To reduce the vertical deflection of the cantilevers, stiff cantilevers with spring constant approx. 120-180 pN/nm are chosen for the stereographic pulling process, in particular for biotin-glass experiments where high rupture forces are obtained. When analyzing the  $z$ -extension and  $x$ -extension of the PEG chain for  $60^\circ$  at 100 nm/s ( $n = 50$ ) we find that the real pulling angle (with all possible inaccuracies) is  $61 (\pm 3)^\circ$ , in good agreement with the preset value.

**Same pulling angle but different pulling directions.** For a given pulling angle, the pulling direction could be different for each pulling event (rotational degree of freedom, Fig. S3b). This may yield different rupture forces for very asymmetric systems (e.g., in receptor-ligand binding). In this study, we ignore this effect because the single chemical

bond (anchor) may be regarded as symmetric in our pulling process.

**Accuracy of the piezo systems.** Whether the polymer can be stretched with the preset angle depends on the accuracy of the piezo systems. We analyze 100 pulling events for a certain angle (here  $45^\circ$  at 100 nm/s) and find that the real pulling angle is at  $46 (\pm 0.1)^\circ$ . This indicates that the piezo system could well work with nanometer accuracy.

Note that in the fixed-pathway scenario, only the vertical components of the results are used for analysis, which are obtained directly from the values recorded by AFM. Therefore, the pulling-angle associated errors (e.g., pulling geometry and direction) do not represent a confounding effect in that case.

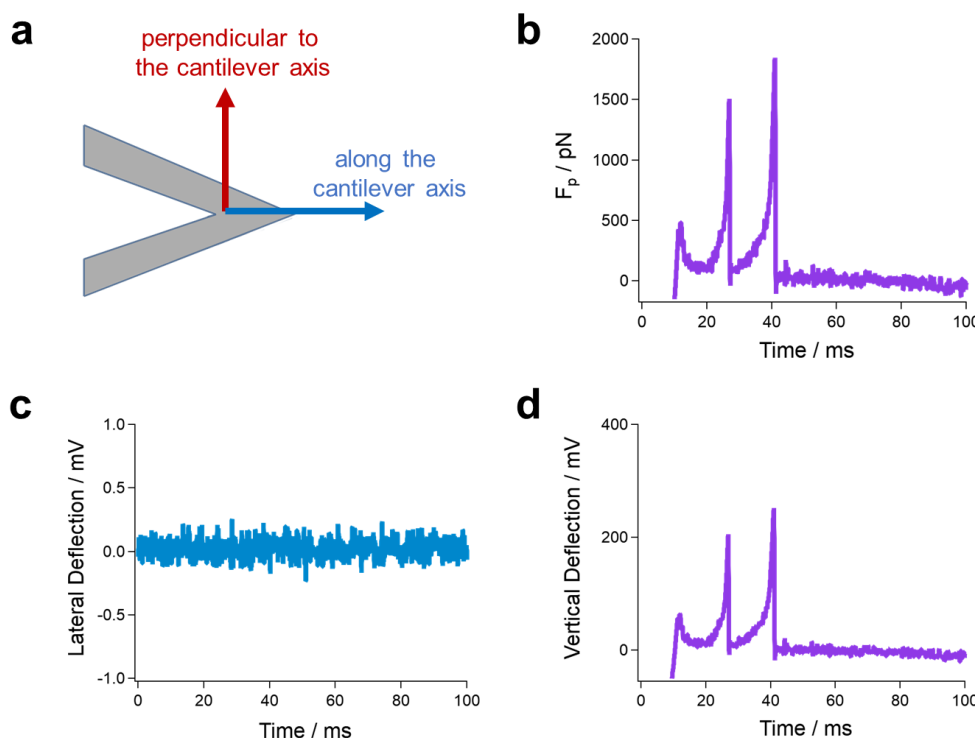


**Fig. S2 Lateral deflection for lateral pulling of single molecules.** (a) Scheme of a cantilever with a definition of different pulling directions given by arrows (the red arrow represents the pulling direction in this study). Although the lateral spring constant of the cantilever (approx.  $10^4$ - $10^5$  pN/nm) is far higher than the vertical spring constant (approx.  $10^2$  pN/nm), the cantilever can still be laterally deflected for sufficiently high lateral force.<sup>4, 5</sup> Due to the geometry of the setup, the lateral force is the strongest for pulling at  $\theta = 60^\circ$  relative to the vertical direction pulling in our study. (b) A typical force-time curve for pulling at  $\theta = 60^\circ$ . The maximum lateral and vertical force applied on the cantilever are 1591 pN and 919 pN, respectively. However, the (c) lateral deflection of the cantilever is below the noise level, while (d) the vertical deflection shows clear single-molecule pulling signatures well above the noise level. These results show that the lateral force in our study is too low to laterally deflect the cantilever appreciably. Therefore, the torsion perpendicular to the cantilever axis can also be neglected in the analysis.

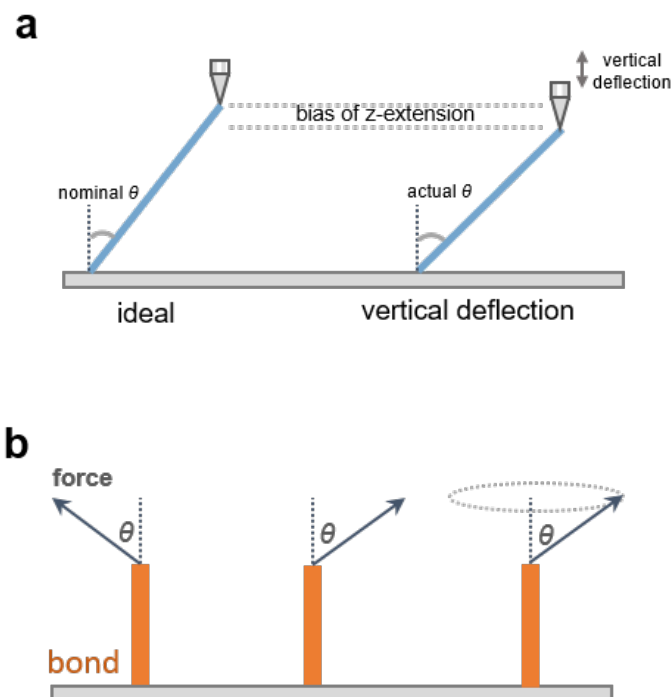


**Fig. S3 Possible effects for stereographic pulling. (a)** The vertical deflection of a cantilever with finite stiffness will cause a shorter z-extension of the polymer than the z-distance driven by the piezo system, leading to a bias due to the pulling geometry for the actual pulling angle at high forces. This effect decreases with increasing cantilever stiffness. Note that the lateral force component applied on the cantilever is perpendicular to the cantilever axis. **(b)** For a given pulling angle, the pulling direction could be different for each pulling event. We ignore this effect because in the presented cases, the single chemical bond (anchor) could be regarded as rotationally symmetric. A detailed discussion can be found in *Analysis of various effects in stereographic pulling* on pages S3-S4.

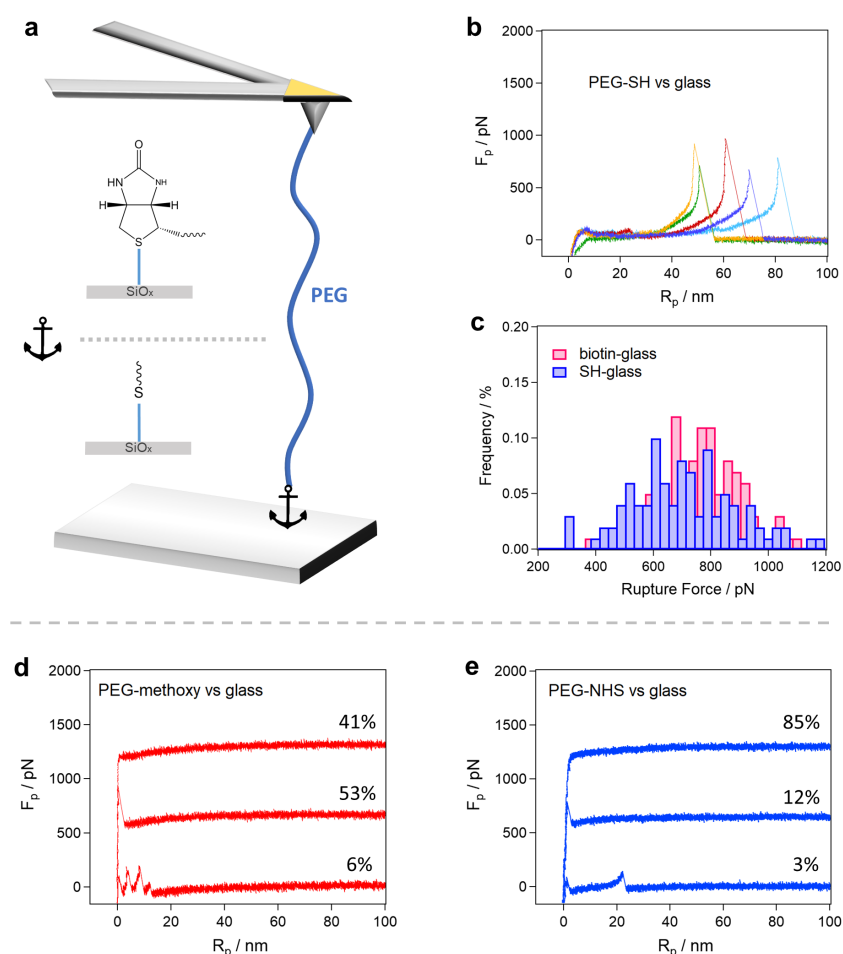


**Fig. S4 Three more systems (thiol-glass, methoxy-glass and NHS-glass) are used to validate the formation of the anchor bond.** Here, all the force measurements are carried out for  $\theta = 0^\circ$  at 100 nm/s in H<sub>2</sub>O. **(a)** Scheme of the experimental scenario. **(b)** Typical force-extension curves ( $F_p$  vs  $R_p$ ) of PEG-thiol on glass substrate with an indentation/contact force of approx. 2.5 nN. Note that  $F_p = F_z$  and  $R_p = R_z$  for  $\theta = 0^\circ$ . **(c)** Statistics of the anchor rupture forces. The mean forces are 767 ( $\pm$  133) pN and 694 ( $\pm$  188) pN for biotin-glass and thiol-glass, respectively (200 out of 1400 curves). **(d-e)** Exemplary different types of force-extension curves and their frequencies of PEG-methoxy (1217 curves) and PEG-NHS (1000 curves) on glass substrate in H<sub>2</sub>O with indentation force ranging from 2.5-10 nN. We could not observe any specific high force single molecule rupture events in those cases. As the only difference among the three experiments (methoxy, NHS and thiol) is the thiol group, the clear difference in the rupture force validates the formation of thiol-glass bonds<sup>6-8</sup> at the applied indentation/ contact force.

## Single-chain elasticity model

In an ideal state, the entropic elastic response of PEG for a pulling force  $F$  can be described by the freely rotating chain (FRC) model, where the relationship between the extension  $R$  and the contour length  $L_0$  is given by<sup>9</sup>

$$R = L_0 \cdot \left[ 1 - \frac{k_B T}{2F l_b} \right] \quad (S1)$$

with  $l_b$  denoting the rotating unit length. However, at high forces, the bond angle/length will be overstretched, leading to a force-dependent contour length  $L(F)$  instead of the constant contour length  $L_0$ .<sup>10</sup> In 2017, Liese et al. determined  $L(F)$  of PEG via *ab initio* quantum chemistry calculations:<sup>11</sup>

$$L(F) = \left( \frac{F}{\gamma} + 1 \right) \cdot L_0 \quad (S2)$$

where the elastic stretching modulus  $\gamma$  is 89 nN. The model combining Eqs. (S1) and (S2) together is called the QM-FRC model:<sup>12</sup>

$$R = \left( \frac{F}{\gamma} + 1 \right) \cdot L_0 \cdot \left[ 1 - \frac{k_B T}{2F l_b} \right] \quad (S3)$$

However, in an aqueous environment, the formation/dissociation of H<sub>2</sub>O bridges among the PEG repeating units will lead to the transition of PEG repeating units between trans and gauche states.<sup>11</sup> Since the two states have different lengths, the contour length  $L_0$  of the whole PEG chain will be altered. Taking the kinetics of the H<sub>2</sub>O bridges into account, the PEG contour length  $L_{TS}(F)$  at a given force can be calculated by:

$$L_{TS}(F) = N \cdot \left[ \frac{l_g}{e^{(-\Delta G + F\Delta L)/k_B T} + 1} + \frac{l_t}{e^{(\Delta G - F\Delta L)/k_B T} + 1} \right] \quad (S4)$$

where  $N$  is the number of monomers,  $l_t$  and  $l_g$  are the length of PEG repeating unit in trans and gauche state respectively, and  $\Delta G$  and  $\Delta L$  are the free energy difference and length difference between the two states respectively. Combining this two-state (TS) model with the QM-FRC model, we finally get the TSQM-FRC model, where the normalized extension  $R_N(F)$  is given by:<sup>12</sup>

$$R_N(F) = \left[ \frac{l_g}{e^{(-\Delta G + F\Delta L)/k_B T} + 1} + \frac{l_t}{e^{(\Delta G - F\Delta L)/k_B T} + 1} \right] \cdot \left( \frac{F}{\gamma} + 1 \right) \cdot \left[ 1 - \frac{k_B T}{2F l_b} \right] \cdot l_t^{-1} \quad (S5)$$

Herein, the kinetics of the H<sub>2</sub>O bridges, the conformational change of PEG at low forces, and the bond angle/length change of PEG at high forces are integrated together, which

therefore could be used to describe the elastic behavior of PEG in the whole force range. Note that  $N l_t$  is used to normalize the PEG chain contour length at infinite force (trans configuration for the whole PEG chain).

The structural parameters of PEG and  $\gamma$  are taken from the paper by Liese et al.:<sup>11</sup>

$l_g = 0.282$  nm (O-C-C-O in gauche state),

$l_t = 0.356$  nm (O-C-C-O in trans state),

$\Delta L = l_t - l_g$ ,  $\gamma = 89$  nN.

According to the definition of the FRC model, each bond freely rotates around the adjacent bonds. Considering that the bonds forming the PEG backbone are heterogeneous (O-C, C-C, C-O), we take the rotating unit length to be  $l_b = 0.146$  nm, i.e., the average bond length of a PEG backbone.<sup>13</sup>

The only remaining parameter is therefore  $\Delta G$ , which is determined via fit to be  $\Delta G = 3.6 k_B T$ , in agreement with the previous reports (3 to 4  $k_B T$ ).<sup>11, 14</sup>

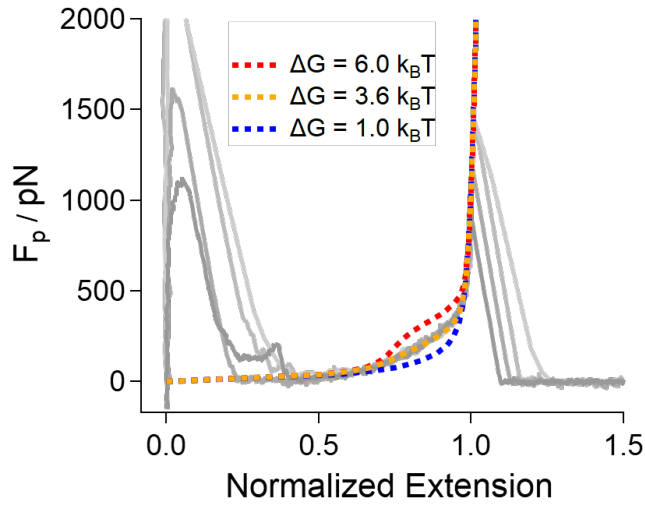


**Fig. S5 TSQM-FRC model fit quality.** Typical force along the pulling direction vs normalized extension ( $F_p$  vs normalized extension, here normalized with extension value at 1000 pN) curves of PEG (grey lines) for  $\theta = 0^\circ$  (vertical pulling, biotin-glass experiments) are compared to the TSQM-FRC fit curves (from Eq. S5) with different  $\Delta G$ . The best fit result is found at  $\Delta G = 3.6 k_B T$ .

## Normalization of the polymer extension

The normalized extension  $R_N(F)$ , defined as the PEG extension  $R$  normalized by  $N l_t$ , can be predicted by the TSQM-FRC model. At high forces (above 500 pN), the PEG chain is fully stretched and almost all H<sub>2</sub>O bridges are dissociated. Thus, the PEG elastic response in this region is dominated by the elastic stretching modulus  $\gamma$  of PEG, which is a model-independent value obtained by quantum mechanical calculations.

If the highest rupture forces are lower than 1000 pN, the force-extension curves are rescaled to  $R_N$  at the highest peak (also fully dominated by the elastic stretching modulus). For rupture force exceeding 1000 pN the respective extensions are rescaled to  $R_N$  at 1000 pN.

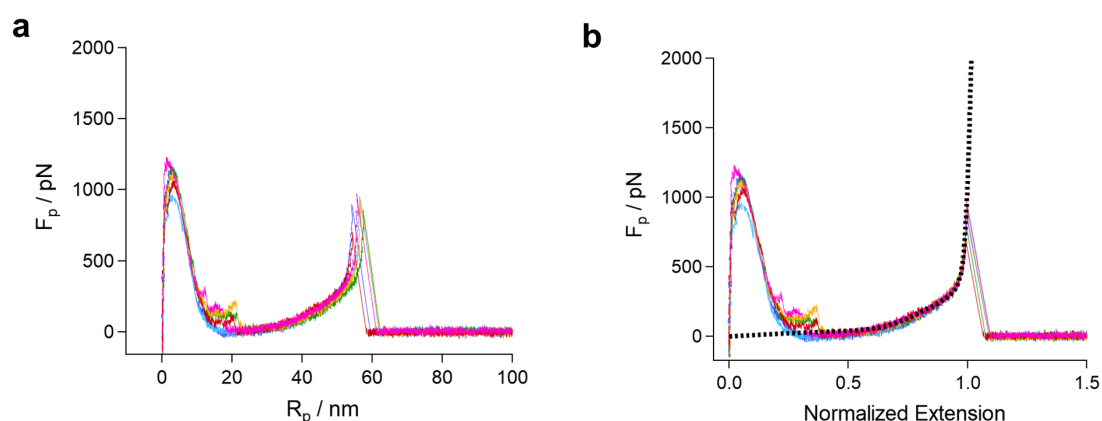


**Fig. S6 Normalization of the extension.** Typical force-extension curves of PEG-biotin on glass in H<sub>2</sub>O (a) before and (b) after normalization of  $R_p$  which is calculated by the TSQM-FRC model curve (represented by black dotted line). The experimental curves shown were obtained for  $\theta = 0^\circ$  (vertical pulling) at 100 nm/s in biotin-glass experiments.

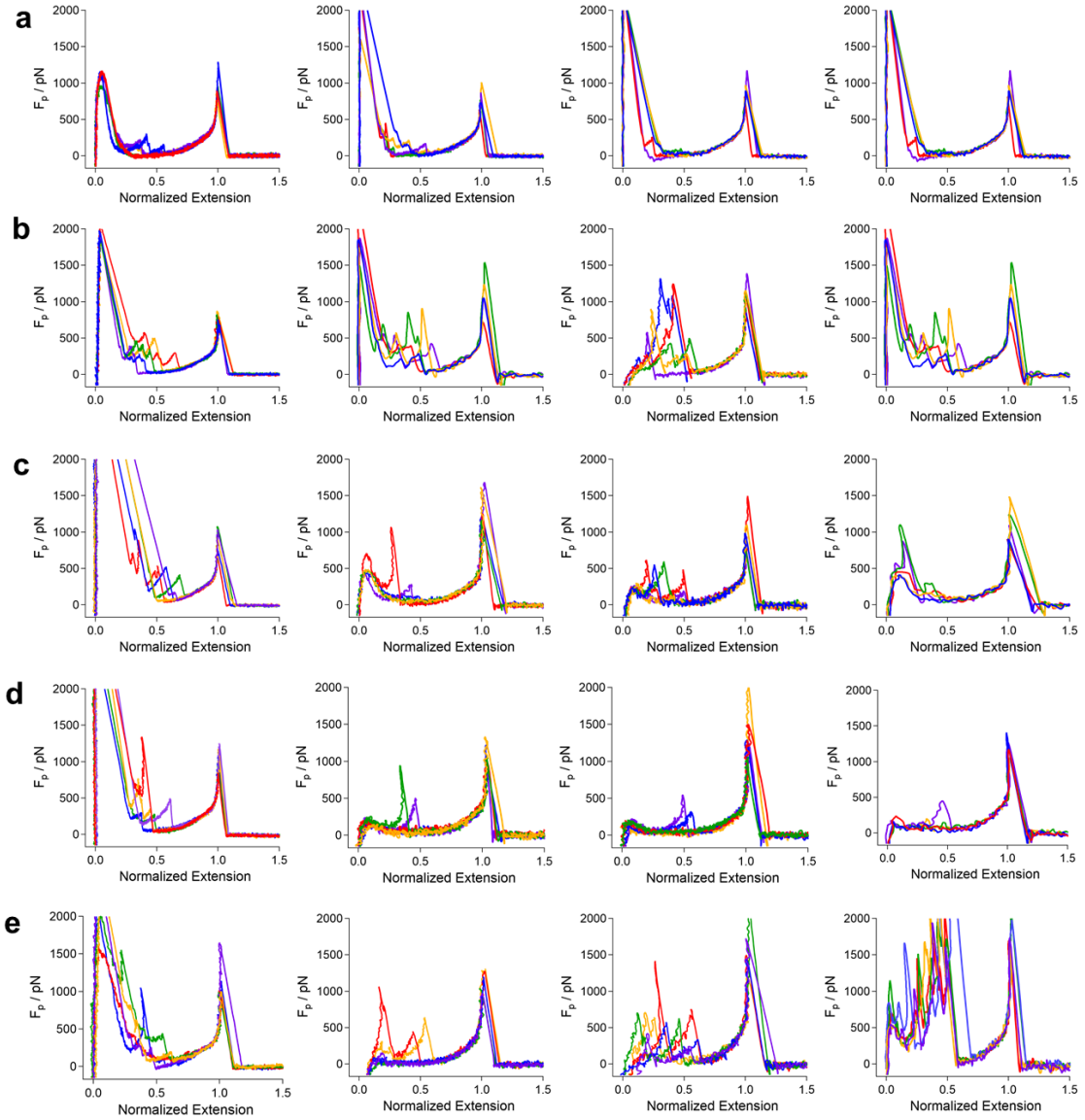


**Fig. S7 Typical normalized reconstructed force-extension curves of PEG-biotin on glass in H<sub>2</sub>O for different pulling angles and velocities. (a) 0° (b) 15° (c) 30° (d) 45° (e) 60°. In each sub-figure, the pulling velocities are 100, 500, 1000, and 5000 nm/s from left to right. The overall success rate for these experiments is approx. 11% ( $n = 2000$  out of 17443 curves).**

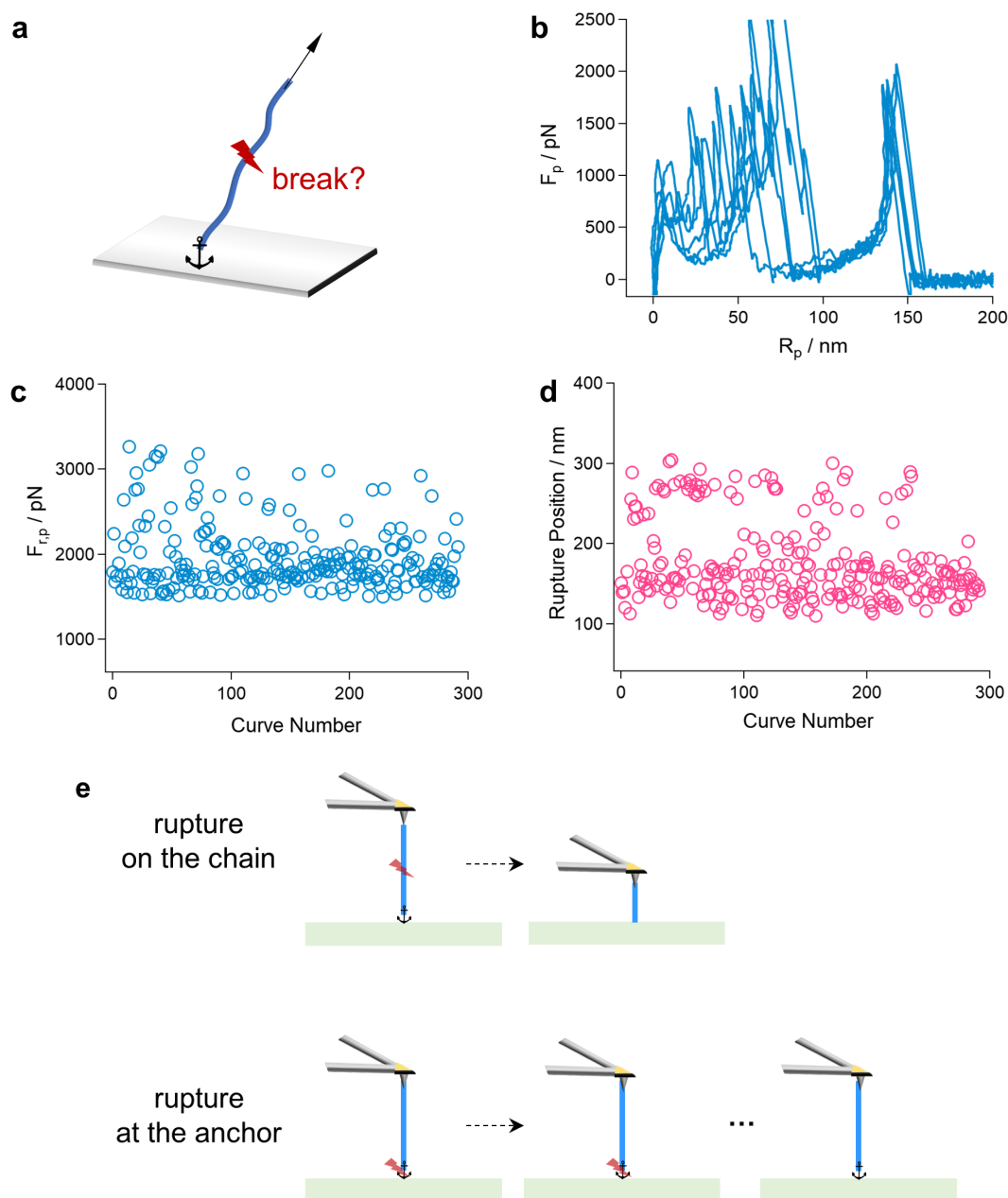


**Fig. S8 Bond rupture happens at the anchor.** (a) A force of approx. 2000 pN is usually associated with the breakage of a covalent bond,<sup>15</sup> which raises concerns that the PEG chain might rupture anywhere between the anchor points upon stretching. (b) Typical reconstructed force-extension curves for PEG-biotin on glass in H<sub>2</sub>O, obtained for  $\theta = 60^\circ$  at 5000 nm/s pulling. Statistics shows that both the (c) rupture force and (d) vertical rupture position are stable over hundreds of high rupture force events ( $n = 257$  out of 889 curves,  $F_{r,p} > 1500$  pN), indicating that the PEG chain itself could withstand these high forces.

(e) Scheme of rupture point (red lightning) and the associated polymer chain length (blue line). When covalent bond rupture occurs within the PEG chain, the chain would become shorter and in addition lose its functional group. This would prevent the PEG chain from forming a new covalent bond with the underlying substrate. Hence, no specific rupture events at high forces would be observed for the following force-extension curves. When covalent bond rupture occurs at the anchor bond, the polymer stays intact and the force-extension curves can be repeated with the same force-extension signature for hundreds of consecutive curves. Therefore, the bond rupture occurs at the biotin-glass anchor bond in our system.

# Rupture force data analysis

**1. DHS model fitting with maximum-likelihood method.** The Dudko–Hummer–Szabo (DHS) model is used to analyze the measured rupture forces  $\{F_n\}_{n=1,2,\dots}$  and the associated loading rates, and thus extract the kinetics of the anchor bond in this study. The functional form of the force-dependent escape rate  $k(F)$  and the associated rupture force distribution  $p(F|\dot{F})$  predicted by the DHS model are as follows:<sup>16</sup>

$$k(F) = k_0 \left[ 1 - \frac{F}{F_c} \right]^{\frac{1}{v}-1} \exp \left( \beta \Delta G_u \left[ 1 - \left( 1 - \frac{F}{F_c} \right)^{\frac{1}{v}} \right] \right) \quad (\text{S6})$$

$$p(F|\dot{F}) = \frac{k(F)}{\dot{F}} \exp \left( -\frac{k_0}{\beta x_u \dot{F}} \left[ \exp \left( \beta \Delta G_u \left[ 1 - \left( 1 - \frac{F}{F_c} \right)^{\frac{1}{v}} \right] \right) - 1 \right] \right) \quad (\text{S7})$$

where  $k_0 = k(F = 0)$  denotes the spontaneous escape rate,  $\Delta G_u$  is the height of the free energy barrier,  $x_u$  is the distance from the bound state to the barrier,  $\dot{F}$  is the loading rate associated with the rupture force  $F$ ,  $\beta = 1/(k_B T)$  is the inverse of the Boltzmann constant times the absolute temperature, and  $F_c = \Delta G_u / (v x_u)$  denotes the critical rupture force. The parameter  $v$  depends on the shape of the underlying free energy landscape:  $v = 1/2$  and  $2/3$  correspond to cusp-like and linear-cubic landscapes respectively, while for  $v = 1$  the Bell-Evans model is recovered.

The fit parameters  $\{\beta \Delta G_u, x_u, k_0\}$  of the DHS model are determined via maximum likelihood estimation by minimizing the negative log-likelihood<sup>17</sup>

$$L(\beta \Delta G_u, x_u, k_0 | \{F_n, \dot{F}_n\}_{n=1,\dots,N}) = - \sum_{n=1}^N \ln(p(F_n | \dot{F}_n)). \quad (\text{S8})$$

Finding the minimum of Eq. S8 requires us to set its derivatives with respect to the model parameters equal to zero but, in most cases, the resulting equations cannot be solved analytically and minimization has to follow numerically. Fortunately, in our case, the equation for  $k_0$  is analytically tractable, giving:

$$k_0 = \left[ \frac{1}{N} \sum_{n=1}^N \frac{1}{\beta x_u \dot{F}_n} \left[ \exp \left( \beta \Delta G_u \left[ 1 - \left( 1 - \frac{F_n}{F_c} \right)^{\frac{1}{v}} \right] \right) - 1 \right] \right]^{-1}. \quad (\text{S9})$$

By plugging this equation into Eq. S8, we reduce our three-dimensional optimization problem, i.e., minimizing Eq. S8 with respect to  $\{\beta\Delta G_u, x_u, k_0\}$ , to an effectively two dimensional one. The associated reduced negative log-likelihood for the remaining two parameters reads then:

$$\begin{aligned}
L(\beta\Delta G_u, x_u | \{F_n, \dot{F}_n\}_{n=1, \dots, N}) \\
= N \ln \left( \sum_{n=1}^N \frac{1}{\beta x_u \dot{F}_n} \left[ \exp \left( \beta\Delta G_u \left[ 1 - \left( 1 - \frac{F_n}{F_c} \right)^{\frac{1}{v}} \right] \right) - 1 \right] \right. \\
\left. - \sum_{n=1}^N \left[ \left( \frac{1}{v} - 1 \right) \ln \left( 1 - \frac{F_n}{F_c} \right) + \beta\Delta G_u \left[ 1 - \left( 1 - \frac{F_n}{F_c} \right)^{\frac{1}{v}} \right] \right] \right). \quad (\text{S10})
\end{aligned}$$

Parameter estimation therefore involves the numerical minimization of Eq. S10 with respect to  $\beta\Delta G_u$  and  $x_u$ , after which the resulting parameter estimates for  $\{\beta\Delta G_u, x_u\}$  are plugged into Eq. S9 to obtain an estimate for  $k_0$ . This leads to a more stable and faster numerical optimization than working directly with Eq. S8. We rely on bootstrapping to gauge the uncertainty of the estimates, by generating new data sets repeatedly from our sample of rupture forces and analyzing the results. We use the resulting variances in parameter estimates to characterize said uncertainties.

**2. Optimizing the fit quality with a systematic protocol.** Rare outliers that are presumably due to, e.g., an unusual bonding state of the anchor, give rise to unusually broad distributions and impair the fit quality. Therefore, we have developed a systematic protocol for trimming rupture force data vs loading rate sets that considers the evolution of the fit parameters with respect to the amount of data points being removed. In order to trim the data set uniformly for all loading rates, we consider subsamples of our data, characterized by the pulling angle and speed, and remove equally many points from each of them. Of course, as more points get removed, one eventually starts throwing meaningful data away, so a threshold is required to stop the trimming procedure. Figs. S9a and S9b demonstrate how the parameter estimates change monotonically with the amount of data points being removed from the analysis. For both the biotin-glass and catechol-TiO<sub>2</sub> data, we see a clear transition between a

regime, where removing points improves the fit, and an open-ended range, where parameter changes are driven by the fact that the sample distributions are gradually becoming thinner. This trend is confirmed by the mean rupture force, as predicted by the DHS model:<sup>16, 18</sup>

$$\langle F \rangle(\dot{F}) = \int_0^\infty dF \cdot F \cdot p(F|\dot{F}) \approx F_c \left( 1 - \left[ 1 - \frac{\exp\left(\frac{k_0}{\beta x_u \dot{F}}\right)}{\beta \Delta G_u} E_1\left(\frac{k_0}{\beta x_u \dot{F}}\right) \right]^v \right), \quad (\text{S11})$$

which only changes significantly with the removal of the first few data points (see Figs. S9c and S9d). Here  $E_1(z) = \int_z^\infty \frac{e^{-y}}{y} dy$  is the exponential integral. It thus seems appropriate to choose the above-mentioned transition point as a threshold to stop the trimming process.

Note that all parameter fits have been exclusively conducted using the above-described maximum likelihood method. The mean rupture force obtained by Eq. S11 and the associated variance (with an improved prefactor to retrieve the correct result for  $v = 1$ )<sup>18</sup>

$$\sigma(\dot{F})^2 \approx \frac{\pi^2}{6} \left( \beta x_u \left[ 1 + \frac{k_0}{\beta x_u \dot{F}} \right] \right)^{-2} \left[ 1 - \frac{\exp\left(\frac{k_0}{\beta x_u \dot{F}}\right)}{\beta \Delta G_u} E_1\left(\frac{k_0}{\beta x_u \dot{F}}\right) \right]^{2v-2} \quad (\text{S12})$$

are only evaluated to visualize the quality of our fit.

The determination of rupture force and loading rate from the experiments are shown in Figs. S9e, and S9f. The parameter estimates for the biotin-glass anchor bond under each pulling angle in the *aligned-pathway* scenario, and the global fit parameters of all the angles in the *fixed-pathway* scenario are shown in Tables S1 ( $v = 2/3$ , linear-cubic shape) and S2 ( $v = 1/2$ , cusp shape). The same trimming parameters are used for both shapes. Both shape parameters give estimates on the same order of magnitude, so their predictions are consistent.

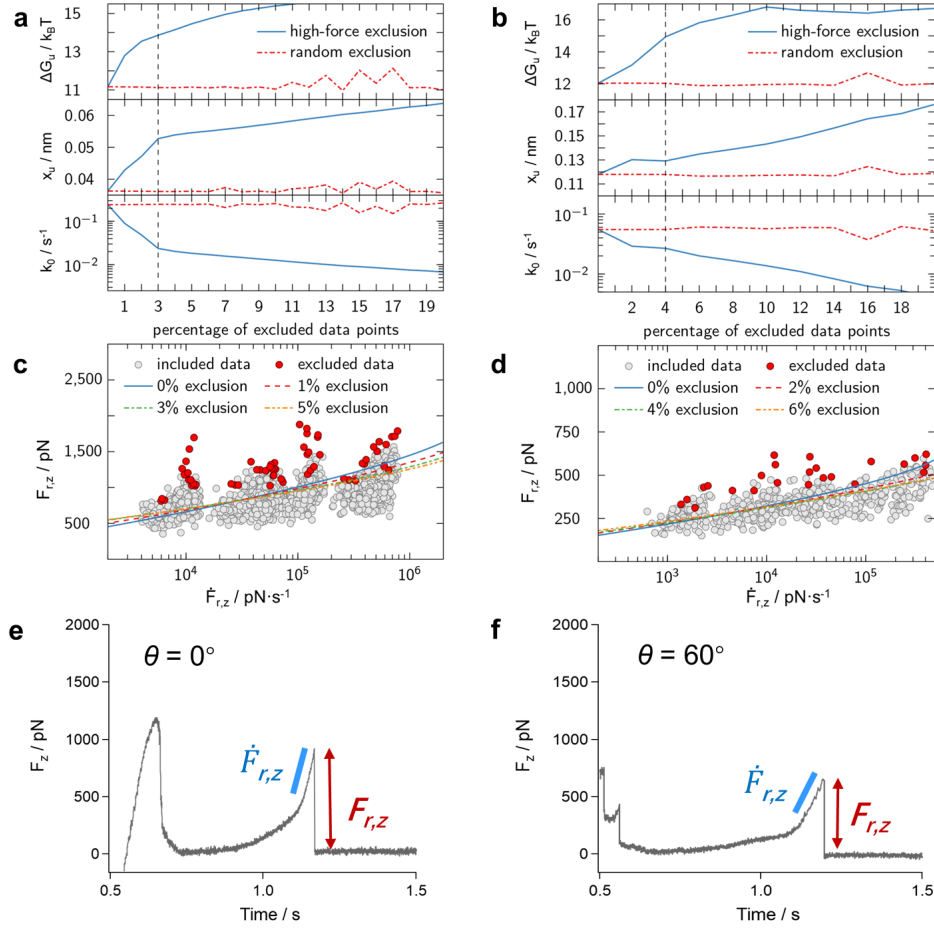


**Fig. S9 Trimming of the rupture force vs loading rate data.** A clear transition (grey dashed line) of the parameters  $\Delta G_u$ ,  $x_u$ ,  $k_0$  can be observed upon trimming (a) 3% of the highest rupture force points for biotin-glass experiments and (b) 4% for catechol-TiO<sub>2</sub> experiments, which is chosen as a threshold to stop the data trimming process. The fit quality reaches a constant level after trimming at this transition point for (c) biotin-glass and (d) catechol-TiO<sub>2</sub> experiments, which is indicative of an optimized fit result (see Tables S1 to S4). (e, f) The rupture force and loading rate are determined as follows: The peak force in the recorded force-time curve is taken as the rupture force  $F_{r,z}$  along the vertical direction, while the linear slope before the peak is taken as the associated loading rate  $\dot{F}_{r,z}$ . Using  $F_{r,p} = F_{r,z} / \cos(\theta)$  and  $\dot{F}_{r,p} = \dot{F}_{r,z} / \cos(\theta)$ , the above-mentioned quantities  $F_{r,z}$  and  $\dot{F}_{r,z}$  are converted to their respective counterparts along the pulling direction. Note that  $F_{r,p} = F_{r,z}$  and  $\dot{F}_{r,p} = \dot{F}_{r,z}$  for  $\theta = 0^\circ$ .

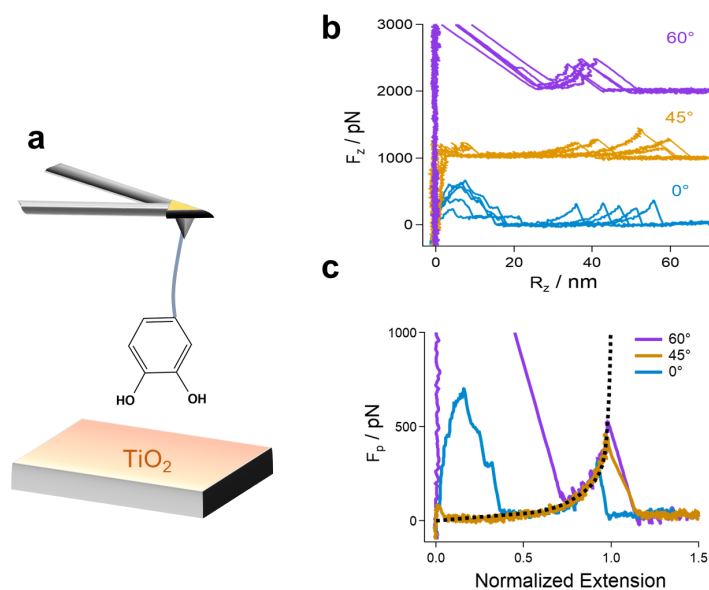


**Fig. S10 Dopamine on TiO<sub>2</sub>.** (a) Dopamine contains a catechol moiety that can be easily oxidized to quinone under high pH and hence leads to different binding modes with TiO<sub>2</sub>.<sup>19</sup> To ensure the formation of catechol-TiO<sub>2</sub> bond, here the experiments are carried out under pH 3, where catechol remains unoxidized. (b) Original recorded vertical force  $F_z$  vs vertical extension  $R_z$  curves of PEG for various angles. (c) After conversion to the force  $F_p$  along the pulling direction and the normalized extension,  $R_N$ , the curves shown in (b) can be superposed. The TSQM-FRC model fit curve ( $\Delta G = 2.2 k_B T$ , black dotted line) is shown as the reference.

Note that the rupture forces of catechol-TiO<sub>2</sub> experiments are only up to 500 pN. Hence, the shape of the kink cannot be observed as clearly as for biotin-glass in pure H<sub>2</sub>O. Furthermore, the elasticity of PEG as well as the kink are dependent on the interactions between the surrounding medium and PEG, which are different in a buffer at pH 3 compared to pure H<sub>2</sub>O. This result is consistent with Krysiak et al.<sup>19</sup>

Aligned-pathway	$\Delta G_u (k_B T)$	$x_u$ (nm)	$k_0 (s^{-1})$
0°	$15.5 \pm 1.4$	$0.056 \pm 0.004$	$0.019 \pm 0.010$
15°	$16.6 \pm 5.4$	$0.071 \pm 0.006$	$0.002 \pm 0.002$
30°	$19.2 \pm 21.9$	$0.040 \pm 0.005$	$0.016 \pm 0.013$
45°	$15.5 \pm 0.5$	$0.043 \pm 0.002$	$0.004 \pm 0.002$
60°	$18.6 \pm 7.2$	$0.033 \pm 0.004$	$0.007 \pm 0.004$
<b>Fixed-pathway</b>			
Global fit of all angles	$13.9 \pm 0.2$	$0.053 \pm 0.001$	$0.024 \pm 0.004$

**Table S1. DHS model fit parameters ( $\nu = 2/3$ , linear-cubic barrier) of biotin-glass bond.** In the table,  $\Delta G_u$  is the height of the energy barrier,  $x_u$  is the distance from the bound state to the barrier,  $k_0$  is the instantaneous escape rate at zero force. Note the results for 0° and global fit are in good agreement with each other.

Aligned-pathway	$\Delta G_u (k_B T)$	$x_u$ (nm)	$k_0 (s^{-1})$
0°	$17.5 \pm 3.2$	$0.063 \pm 0.007$	$0.011 \pm 0.009$
15°	$19.0 \pm 3.4$	$0.085 \pm 0.012$	$0.001 \pm 0.002$
30°	$23.4 \pm 22.7$	$0.041 \pm 0.006$	$0.014 \pm 0.012$
45°	$18.2 \pm 0.7$	$0.058 \pm 0.005$	$0.001 \pm 0.001$
60°	$21.3 \pm 6.1$	$0.036 \pm 0.004$	$0.005 \pm 0.004$
<b>Fixed-pathway</b>			
Global fit of all angles	$15.7 \pm 0.3$	$0.066 \pm 0.003$	$0.008 \pm 0.002$

**Table S2. DHS model fit parameters ( $\nu = 1/2$ , cusp barrier) of biotin-glass bond.** In the table,  $\Delta G_u$  is the height of the energy barrier,  $x_u$  is the distance from the bound state to the barrier,  $k_0$  is the instantaneous escape rate at zero force. Note the results for 0° and global fit are in good agreement with each other.

Aligned-pathway	$\Delta G_u (k_B T)$	$x_u$ (nm)	$k_0 (s^{-1})$
0°	$15.3 \pm 0.7$	$0.148 \pm 0.010$	$0.012 \pm 0.007$
45°	$16.0 \pm 13.5$	$0.075 \pm 0.008$	$0.06 \pm 0.03$
60°	$18.2 \pm 18.6$	$0.066 \pm 0.006$	$0.022 \pm 0.012$
<b>Fixed-pathway</b>			
Global fit of all angles	$14.9 \pm 0.8$	$0.129 \pm 0.007$	$0.027 \pm 0.008$

**Table S3. DHS model fit parameters ( $\nu = 2/3$ , linear-cubic barrier) of catechol-TiO<sub>2</sub> bond.** In the table,  $\Delta G_u$  is the height of the energy barrier,  $x_u$  is the distance from the bound state to the barrier,  $k_0$  is the instantaneous escape rate at zero force. Note the results for 0° and global fit are in good agreement with each other.

Aligned-pathway	$\Delta G_u (k_B T)$	$x_u$ (nm)	$k_0 (s^{-1})$
0°	$17.3 \pm 0.8$	$0.173 \pm 0.017$	$0.006 \pm 0.006$
45°	$17.7 \pm 12.6$	$0.083 \pm 0.012$	$0.043 \pm 0.027$
60°	$20.5 \pm 21.1$	$0.073 \pm 0.011$	$0.015 \pm 0.012$
<b>Fixed-pathway</b>			
Global fit of all angles	$16.7 \pm 1.0$	$0.148 \pm 0.011$	$0.015 \pm 0.007$

**Table S4. DHS model fit parameters ( $\nu = 1/2$ , cusp barrier) of catechol-TiO<sub>2</sub> bond.** In the table,  $\Delta G_u$  is the height of the energy barrier,  $x_u$  is the distance from the bound state to the barrier,  $k_0$  is the instantaneous escape rate at zero force. Note the results for 0° and global fit are in good agreement with each other.

# References

1. F. Kühner, M. Erdmann and H. E. Gaub, *Phys. Rev. Lett.*, 2006, **97**, 218301.
2. J. M. Neumeister and W. A. Ducker, *Rev. Sci. Instrum.*, 1994, **65**, 2527-2531.
3. F. Rico, L. Gonzalez, I. Casuso, M. Puig-Vidal and S. Scheuring, *Science*, 2013, **342**, 741-743.
4. S. A. Edwards, W. A. Ducker and J. E. Sader, *J. Appl. Phys.*, 2008, **103**, 064513.
5. C. P. Green, H. Lioe, J. P. Cleveland, R. Proksch, P. Mulvaney and J. E. Sader, *Rev. Sci. Instrum.*, 2004, **75**, 1988-1996.
6. C. R. Peiris, S. Ciampi, E. M. Dief, J. Zhang, P. J. Canfield, A. P. Le Brun, D. S. Kosov, J. R. Reimers and N. Darwish, *Chem. Sci.*, 2020, **11**, 5246-5256.
7. M. Hu, F. Liu and J. M. Buriak, *ACS Appl. Mater. Interfaces*, 2016, **8**, 11091-11099.
8. J. L. Lou, H. W. Shiu, L. Y. Chang, C. P. Wu, Y.-L. Soo and C.-H. Chen, *Langmuir*, 2011, **27**, 3436-3441.
9. L. Livadaru, R. Netz and H. Kreuzer, *Macromolecules*, 2003, **36**, 3732-3744.
10. T. Hugel, M. Rief, M. Seitz, H. E. Gaub and R. R. Netz, *Phys. Rev. Lett.*, 2005, **94**, 048301.
11. S. Liese, M. Gensler, S. Krysiak, R. Schwarzl, A. Achazi, B. Paulus, T. Hugel, J. r. P. Rabe and R. R. Netz, *ACS Nano*, 2017, **11**, 702-712.
12. W. Cai, S. Lu, J. Wei and S. Cui, *Macromolecules*, 2019, **52**, 7324-7330.
13. Y. Bao, Z. Luo and S. Cui, *Chem. Soc. Rev.*, 2020, **49**, 2799-2827.
14. F. Oesterhelt, M. Rief and H. E. Gaub, *New J. Phys.*, 1999, **1**, 6.1-6.11.
15. M. Grandbois, M. Beyer, M. Rief, H. Clausen-Schaumann and H. E. Gaub, *Science*, 1999, **283**, 1727-1730.
16. O. K. Dudko, G. Hummer and A. Szabo, *Proc. Natl. Acad. Sci.*, 2008, **105**, 15755-15760.
17. S. Getfert and P. Reimann, *Phys. Rev. E*, 2007, **76**, 052901.
18. R. W. Friddle, *Phys. Rev. Lett.*, 2008, **100**, 138302.
19. S. Krysiak, Q. Wei, K. Rischka, A. Hartwig, R. Haag and T. Hugel, *Beilstein J. Org. Chem.*, 2015, **11**, 828-836.